Supporting Information

A new series of 3D lanthanide phenoxy-carboxylate: Synthesis, crystal structure, magnetism and photoluminescence study

Rupam Sen,*, a Sanchayeeta Paul,a Alolika Sarkar,a Alexandre M. P. Botas,b Albano N. Carneiro Neto,b Paula Brandão,c Armandina M. L. Lopes,d Rute A. S. Ferreira,*,b João P. Araújo,d Zhi Lin,*, c

aDepartment of Chemistry, Adamas University, Barasat, Kolkata 700126, India.
e-mail: rupamsen1@yahoo.com
bDepartment of Physics and CICECO – Aveiro Institute of Materials, University of Aveiro, 3810-193, Aveiro, Portugal
e-mail: rferreira@ua.pt
cDepartment of Chemistry and CICECO, University of Aveiro, 3810-193, Aveiro, Portugal
e-mail: zlin@ua.pt
dDepartment of Physics and Astronomy, FCUC, IFIMUP, Institute of Physics for Advanced Materials, Nanotechnology and Photonics, University of Porto, 4169-007 Porto, Portugal

Table of Contents

1. FT-IR analysis

FT-IR spectra of the samples suspended in KBr pellets were recorded on a Perkin–Elmer RX I FT-IR spectrometer under the flow of N_2 at the rate of 20 ml/min and show in Figure S1. The bands observed at 1608 cm^{-1} and 1548 cm^{-1} for **1** (1570 cm^{-1} and 1532 cm^{-1} for **2** and 1608 cm^{-1} and 1548 cm^{-1} for **3**) are attributed to the asymmetric stretching vibrations for carboxylate groups. The characteristic bands observed at 1435 and 1405 cm^{-1} for **1** (1442 and 1381cm^{-1} for **2** and 1442 and 1405 cm^{-1} for **3**) can be regarded as the symmetric stretching vibrations of the carboxylate groups. The band at 3596 cm^{-1} for **1** (3558 cm^{-1} for **2** and 3596 cm^{-1} for **3**) appeared due to the presence of the OH group, while broad bands around 3430 cm^{-1} for all three compounds reveal the presence of water molecules in the compound.

2. Figures
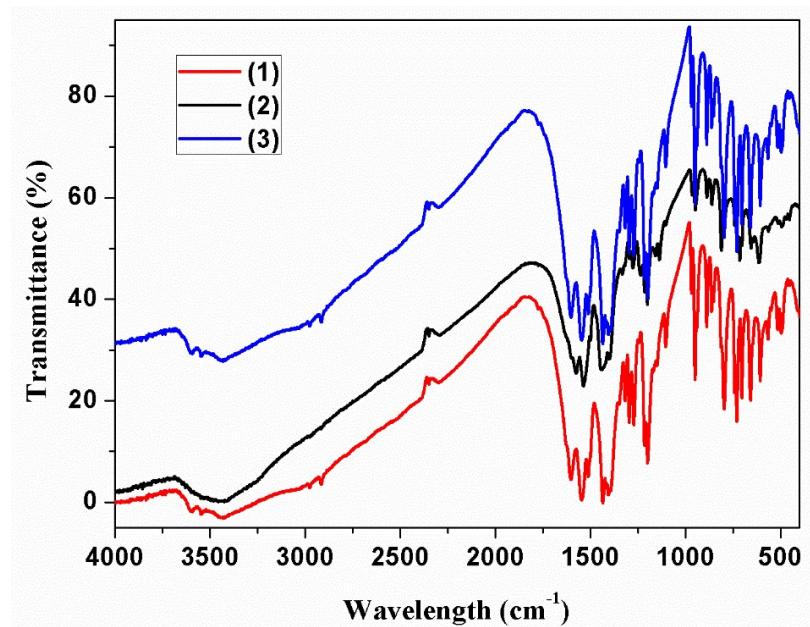
Figure S1. FT-IR spectra of compounds **1**, **2**, and **3**.
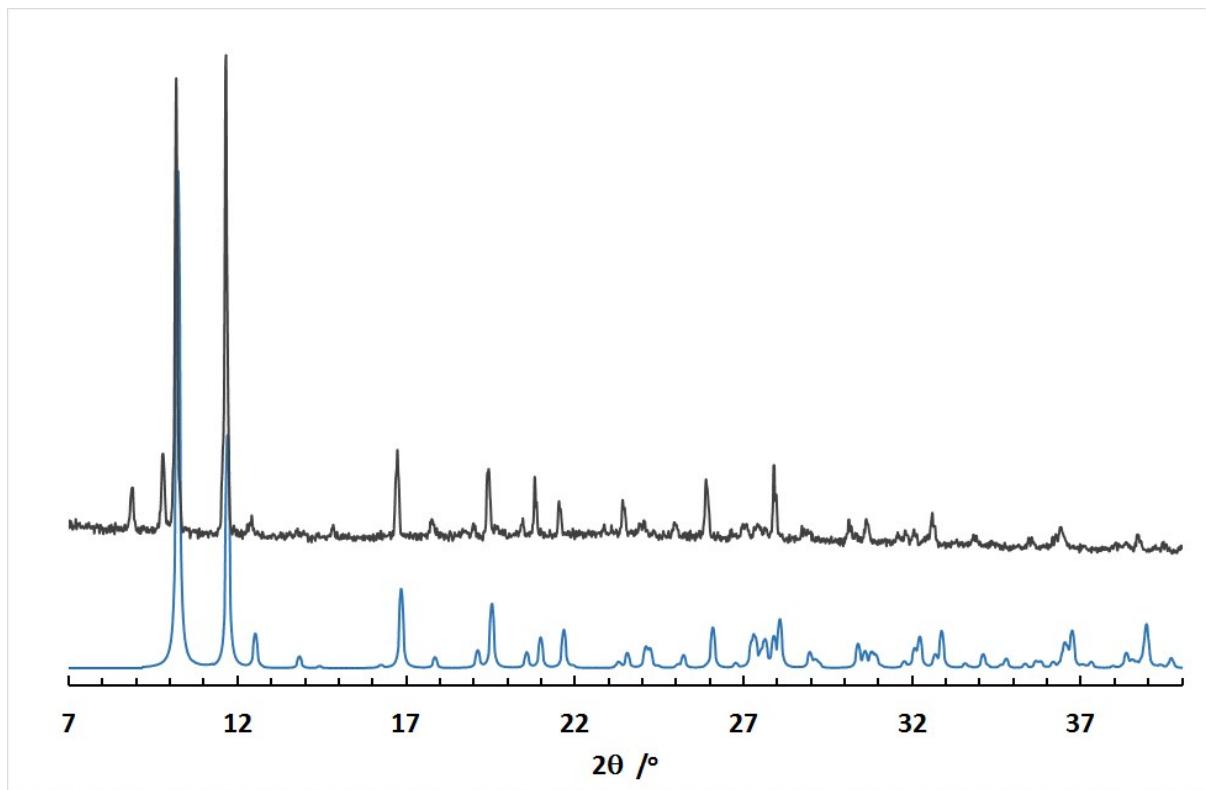
Figure S2. PXRD pattern of **1** (black) and simulated one from single crystal X-ray data (blue).
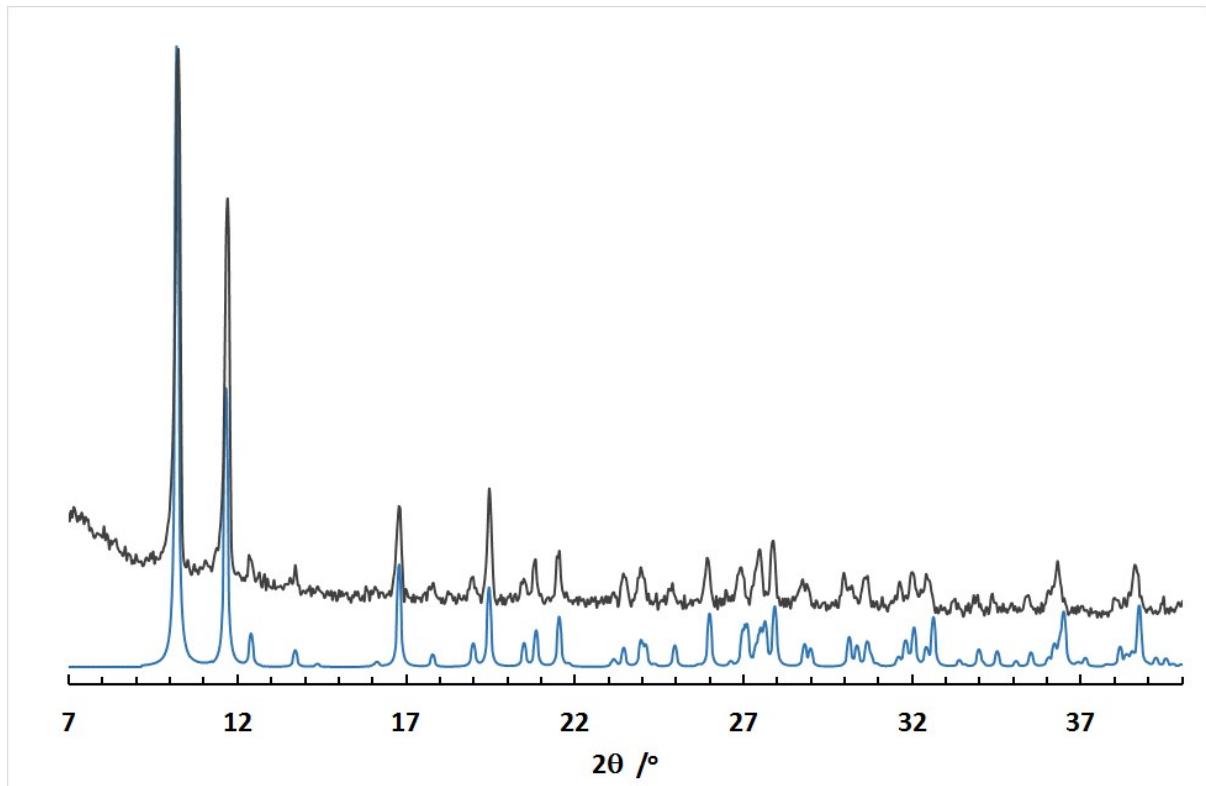
Figure S3. PXRD pattern of **2** (black) and simulated one from single crystal X-ray data (blue).
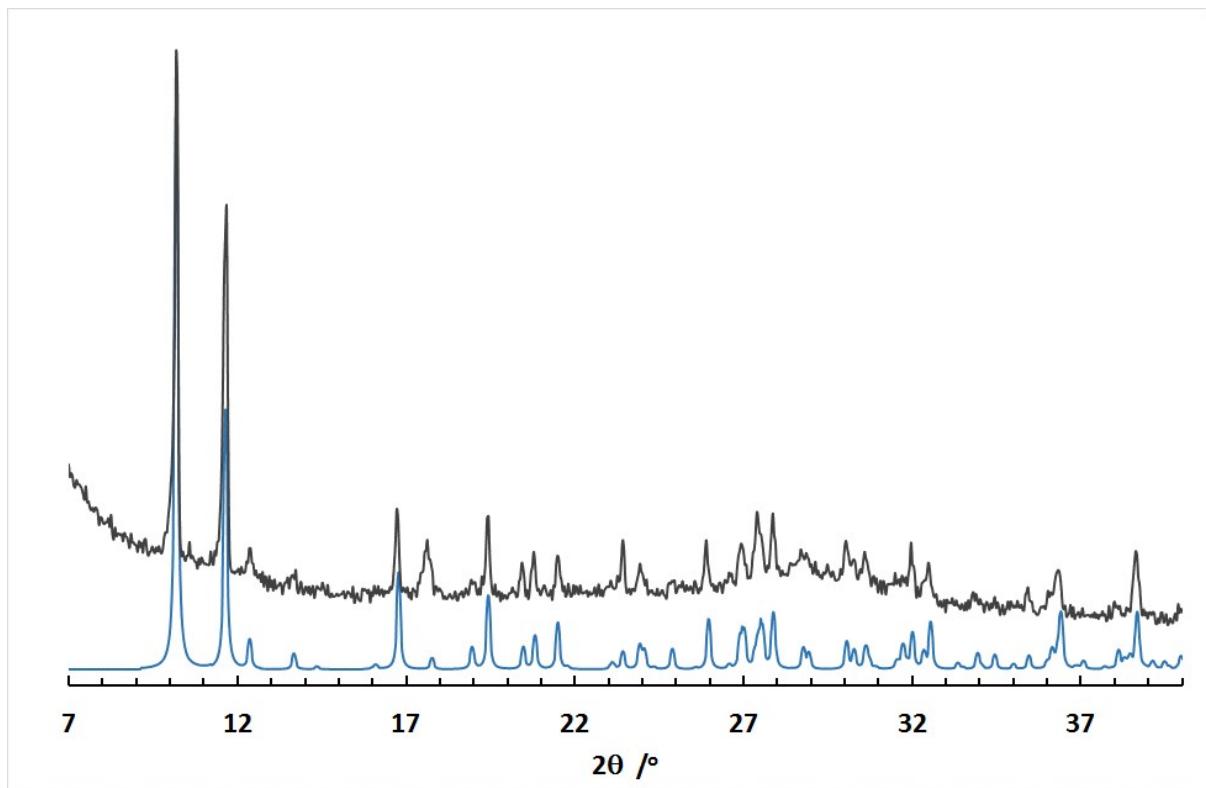
Figure S4. PXRD pattern of **3** (black) and simulated one from single crystal X-ray data (blue).
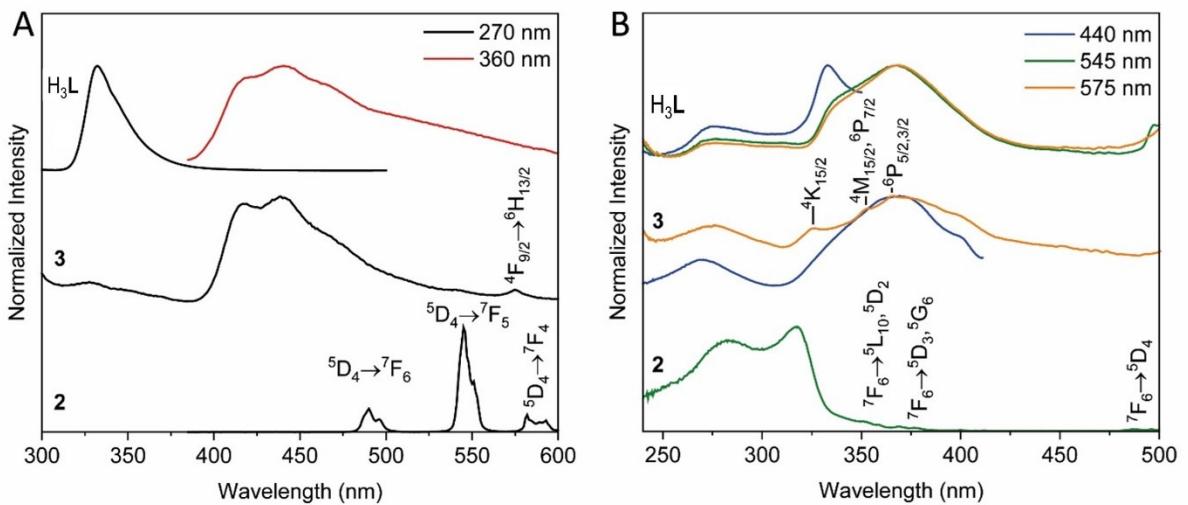
Figure S5. Room-temperature a) emission spectra excited at 270 nm and 360 nm and b) excitation spectra monitored at 440 nm, 545 nm, and 575 nm for **2**, **3**, and free ligand H_3L.
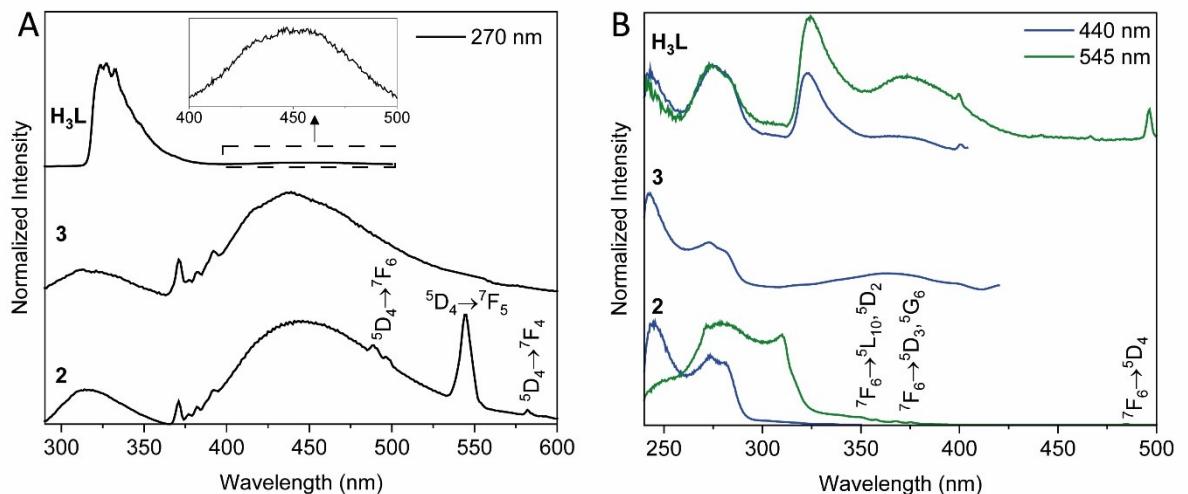
Figure S6. Low-temperature (15 K) a) emission spectra excited at 270 nm and b) excitation spectra monitored at 440 nm and 545 nm for **2**, **3**, and free ligand H_3L. The inset in (a) shows a magnification (x25) of the 400-500 nm range for free ligand H_3L.
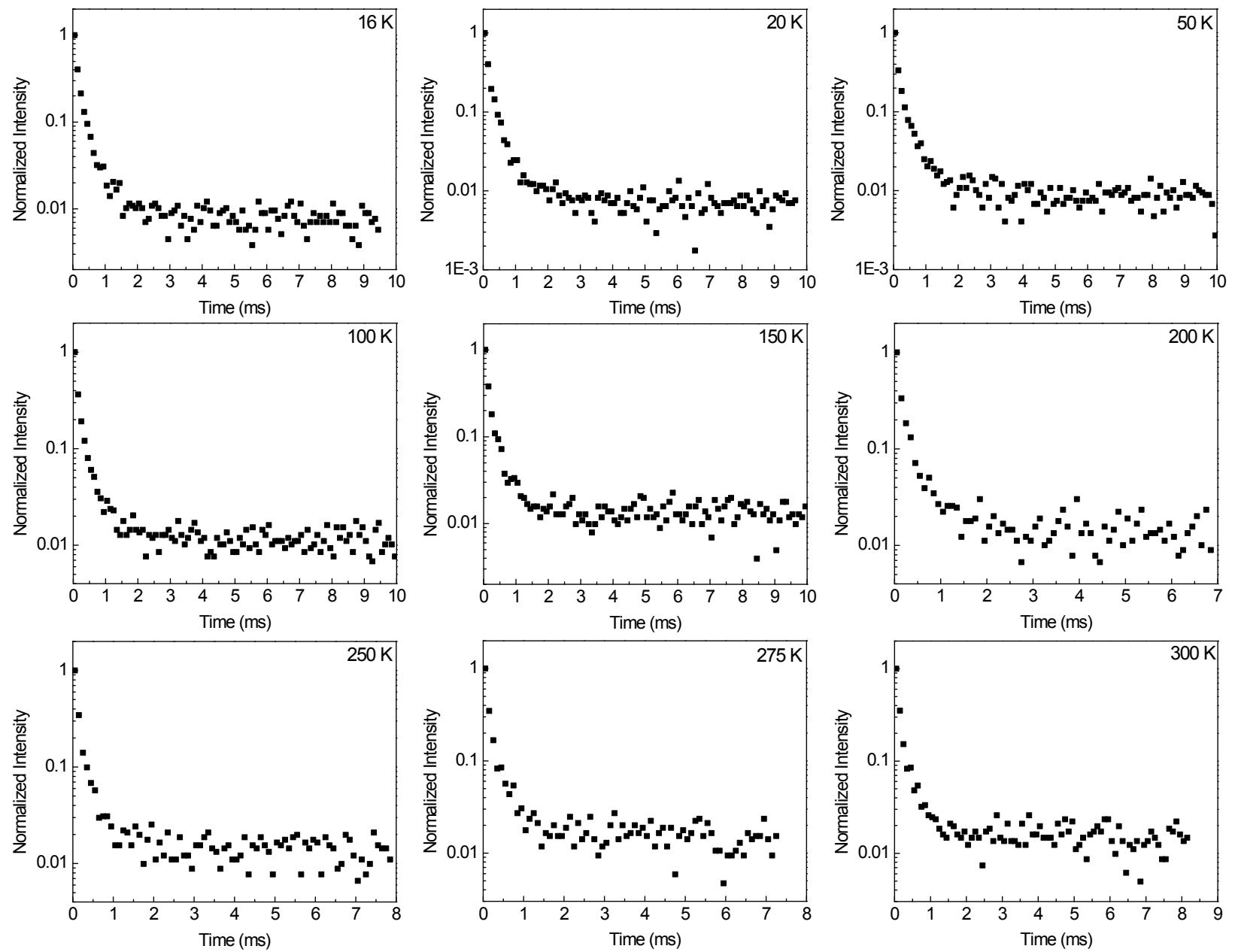
Figure S7. Emission decay curves of **2** excited at 310 nm and monitored at 545 nm as function of the temperature.
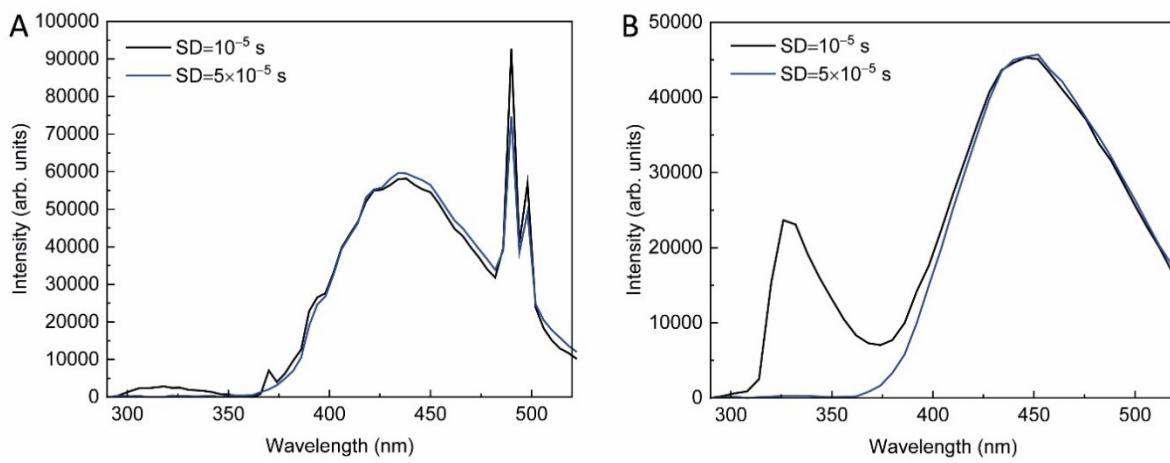
Figure S8. Low-temperature (15 K) time-resolved emission spectra excited at 270 nm for a) **2** and b) free ligand H$_3$**L** acquired at distinct starting delay (SD) values: SD=10^{-5} s and SD=5×10^{-5} s.
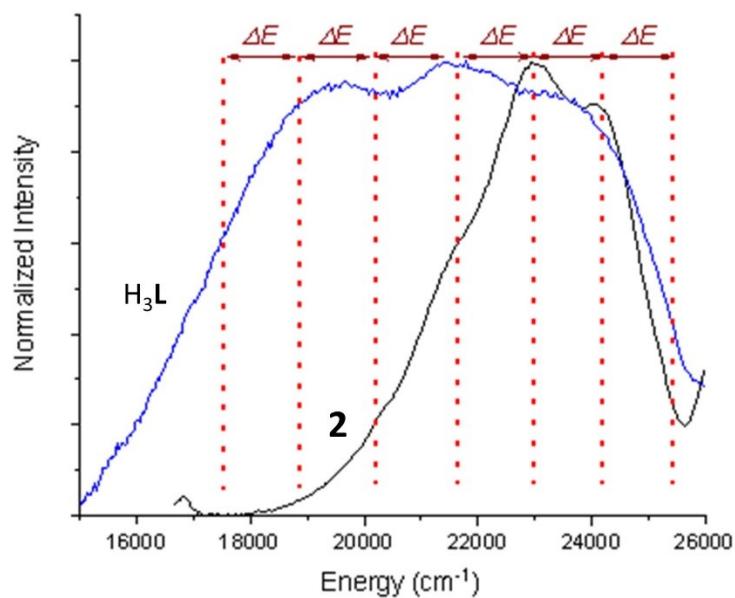
Figure S9. Emission spectra (300 K) excited at 365 nm for free ligand H$_3$**L** and **2**. The vertical lines assign the energy of the vibrational progression characterized by $\Delta E \sim 1300$ cm^{-1}.
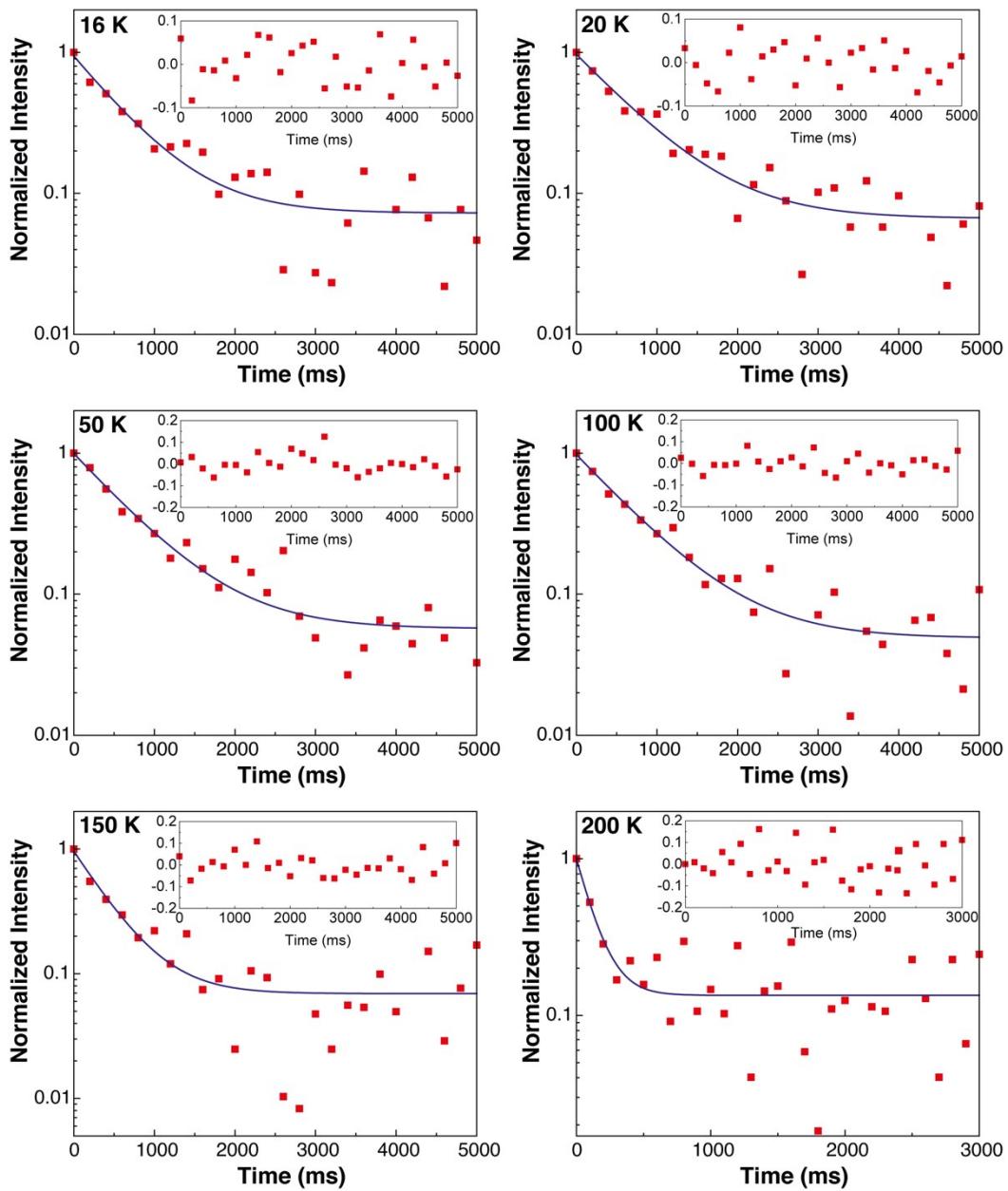
Figure S10. Emission decay curves of **2** excited at 270 nm and monitored at 440 nm as a function of the temperature. The solid lines represent the data best fit using a single exponential function. The insets show the fit residual plots.
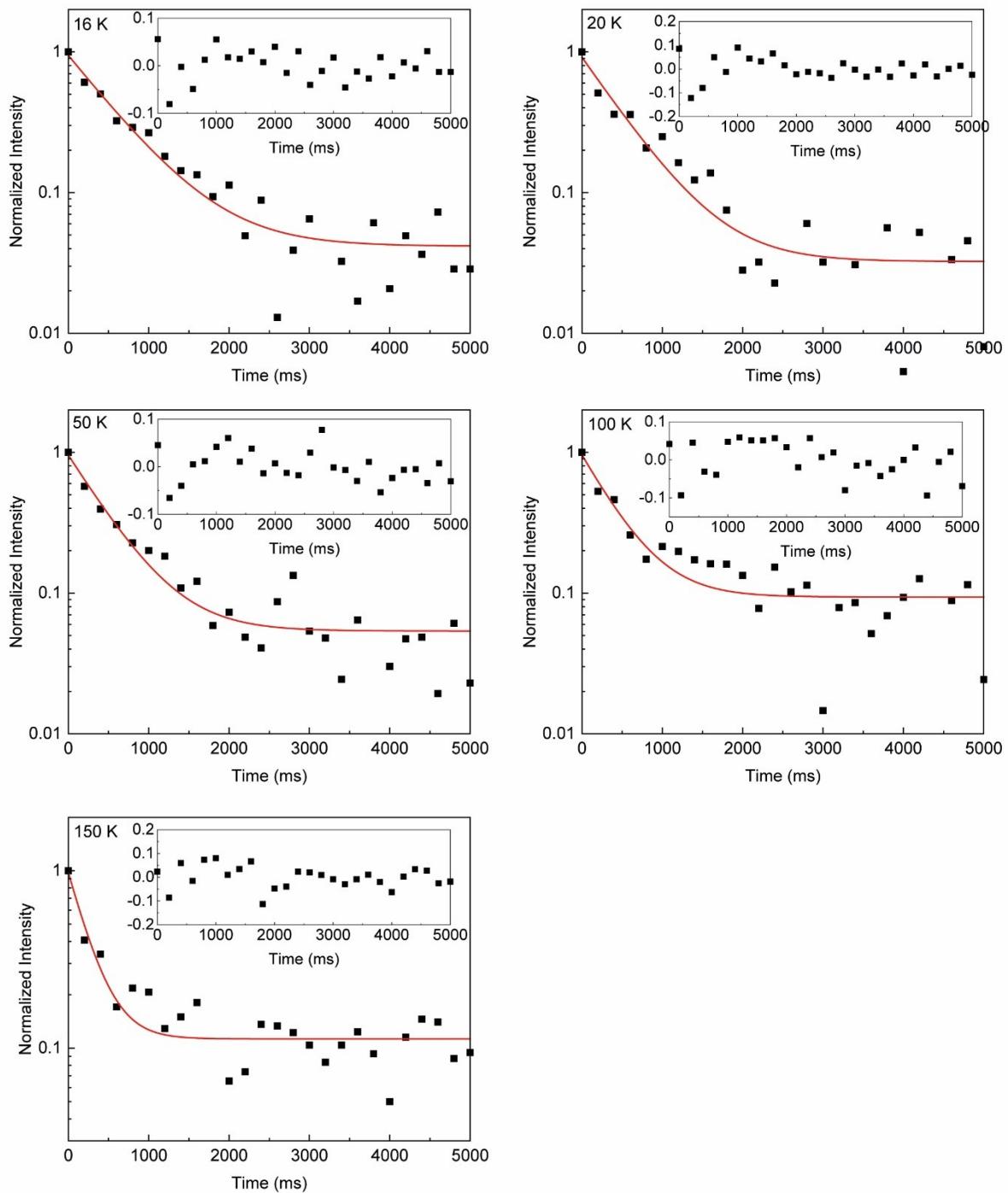
Figure S11. Emission decay curves of free ligand H₃L excited at 270 nm and monitored at 440 nm as a function of the temperature. The solid lines represent the data best fit using a single exponential function. The insets show the fit residual plots.

3. Table

Table S1. Selected bond lengths [Å] and angles [º] for compounds **1** to **3**

Bond distances		Bond angles	
Compound **1**			
La1-O1	2.333(4)	O1-La1-O3	82.9(1)
La1-O3	2.222(4)	O1-La1-O7	69.8(1)
La1-O7	2.321(4)	O2-La1-O3	85.2(1)
La1-O1	2.452(4)	O1-La1-O1	66.5(1)
La1-O2	2.408(4)	O1-La1-O2	115.0(1)
La1-O3	2.277(4)	O1-La1-O3	149.2(1)
La1-O4	2.329(5)	O1-La1-O4	75.8(1)
La1-O5	2.300(4)	O1-La1-O5	126.8(1)
		O3-La1-O7	107.0(1)
		O2-La1-O4	106.7(1)
Compound **2**			
Tb1-O1	2.361(2)	O1-Tb1-O3	82.24(7)
Tb1-O3	2.258(2)	O1-Tb1-O7	69.81(8)
Tb1-O1	2.478(2)	O1-Tb1-O1	67.0(1)
Tb1-O3	2.307(2)	O1-Tb1-O2	115.03(7)
Tb1-O2	2.438(2)	O1-Tb1-O3	149.09(7)
Tb1-O4	2.358(2)	O1-Tb1-O4	75.85(7)
Tb1-O5	2.332(2)	O1-Tb1-O5	126.14(7)
Tb1-O7	2.363(3)	O3-Tb1-O7	107.52(8)
Compound **3**			
Dy1-O1	2.376(2)	O1-Dy1-O3	82.20(8)
Dy1-O3	2.267(2)	O1-Dy1-O7	69.81(8)
Dy1-O7	2.377(3)	O1-Dy1-O1	67.28(7)
Dy1-O1	2.482(2)	O1-Dy1-O2	114.97(8)
Dy1-O2	2.460(2)	O1-Dy1-O3	149.05(8)
Dy1-O3	2.314(2)	O1-Dy1-O4	125.98(8)
Dy1-O4	2.343(2)	O1-Dy1-O5	76.03(7)
Dy1-O5	2.365(2)	O3-Dy1-O7	107.70(8)

O3-Dy1-O2	162.65(8)
O3-Dy1-O3	79.41(8)
O3-Dy1-O4	81.24(8)

Summary of SHAPE analysis for Ln (III) centers in complexes **1 - 3**.

Various probable shapes / geometries for **coordination number 8**:

Vertices	Code	Label	Shape	Symmetry
8	1	OP-8	Octagon	D_{8h}
	2	HPY-8	Heptagonal pyramid	C_{8v}
	3	HBPY-8	Hexagonal bipyramid	D_{6h}
	4	CU-8	Cube	O_h
	5	SAPR-8	Square antiprism	D_{4d}
	6	TDD-8	Triangular dodecahedron	D_{2d}
	7	JGBF-8	Johnson gyrobifastigium J26	D_{2d}
	8	JETBPY-8	Johnson elongated triangular bipyramid J14	D_{3h}
	9	JBTPR-8	Biaugmented trigonal prism	C_{2v}
	10	BTPR-8	Biaugmented trigonal prism	C_{2v}
	11	JSD-8	Snub diphenoid J84	D_{2d}
	12	TT-8	Triakis tetrahedron	T_d
	13	ETBPY-8	Elongated trigonal bipyramid	D_{3h}

Table S2. (Complex-1)

Structure [ML8]   OP-8   HPY-8   HBPY-8   CU-8   SAPR-8   TDD-8   JGBF-8   JETBPY-8   JBTPR-8   BTPR-8   JSD-8   TT-8   ETBPY-8

La1,   29.802,   21.949,   14.399,   9.446,   1.792,   2.964,   13.519,   26.604,   3.281,   2.650,   4.939,   10.168,   21.405

Table S3. (Complex-2)

| Structure [ML8] | OP-8 | HPY-8 | HBPY-8 | CU-8 | SAPR-8 | TDD-8 |
| JGBF-8 | JETBPY-8 | JBTPR-8 | BTPR-8 | JSD-8 | TT-8 | ETBPY-8 |

Tb1, 29.784, 21.966, 14.388, 9.454, 1.804, 2.962, 13.469, 26.627,
3.267, 2.638, 4.929, 10.172, 21.420

Table S4. (Complex-3)

| Structure [ML8] | OP-8 | HPY-8 | HBPY-8 | CU-8 | SAPR-8 | TDD-8 |
| JGBF-8 | JETBPY-8 | JBTPR-8 | BTPR-8 | JSD-8 | TT-8 | ETBPY-8 |

Dy, 29.856, 21.864, 14.347, 9.397, 1.824, 2.987, 13.460, 26.668,
3.306, 2.697, 4.987, 10.091, 21.399

Table S5. Hydrogen bonds present in the compounds **1** to **3**

D–H···A		H···A / Å	D···A / Å	D···H···A /°
	Compound **1**			
O6-H6 ···O2 [-x, -y+1, -z+3]		1.95(7)	2.84(6)	170(7)
	Compound **2**			
O6-H6...O2	[-x,-y+1,-z+3]	1.87(4)	2.847(3)	178(3)
O7-H7A...O5	[x-1,-y+3/2, z-1/2]	1.832(19)	2.650(4)	166(4)
O7-H7B...O100		2.01(3)	2.835(4)	173(3)
O100-H10A...O7 [x, -y+3/2, z-1/2]		2.41(2)	3.140(4)	147(4)
	Compound **3**			
O6-H6 ···O2 [-x+1, -y+1, -z-1]		2.02(5)	2.852(4)	172(4)
O7-H7A···O5 [x+1, -y+1/2, z+1/2]		1.835(19)	2.655(3)	161(4)
O7-H7B…O100		2.01(3)	2.830(4)	160(4)
0100-H10A…O7 [x, -y+1/2, z+1/2]		2.46(3)	3.143(4)	140(5)

4. Theoretical analysis

4.1 In silico experiments

From the crystallographic data, it was extracted the dimeric structure of product **2** (Figure S12) and the canonical molecular orbitals (CMOs) of the excited states (singlet and triplet, Figure S13a) were calculated using the time-dependent DFT in Gaussian 09 revision D.01 program [1]. The functional B3LYP [2,3] was employed together with the 6-311++G(d,p) Pople's basis set [4] to treat O, C, and H atoms for the isolated ligands. The CMO decomposition is useful to estimate where the donor state is localized and, in this way, the donor-acceptor distance (R_L) can be estimated (Figure S13b).
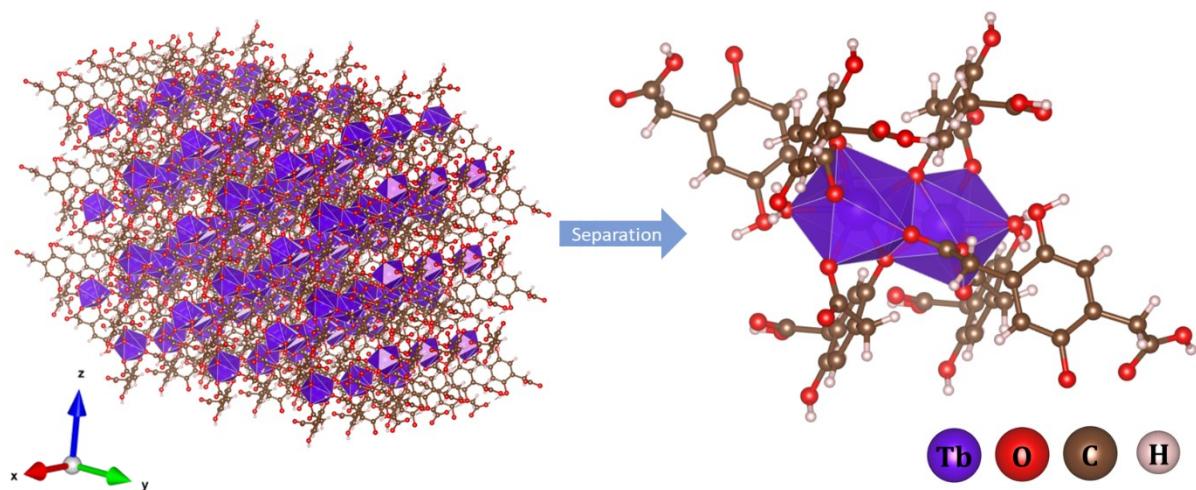
Figure S12. Extraction of the dimer structure for the TD-DFT calculations of singlet and triplet excited states (energy donors). The dimer structure is composed of 6 ligands.
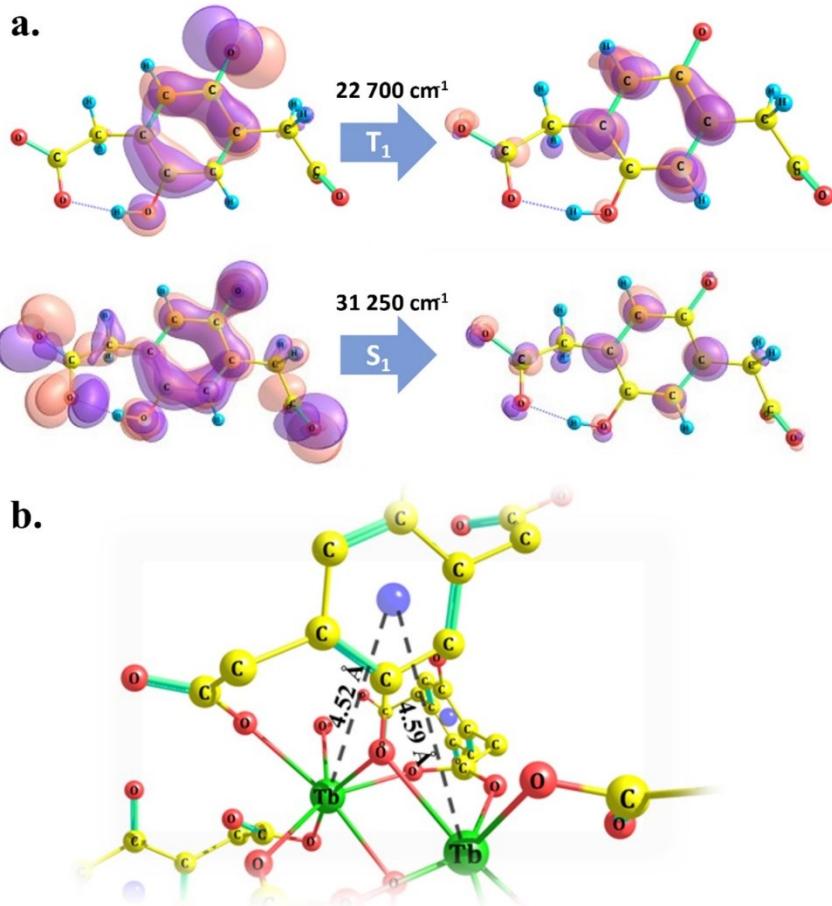
Figure S13. a) MO compositions for the excited T_1 and S_1 states (isosurfaces of 0.04 $e/a_0{}^3$). The centroid of the unoccupied molecular orbitals (on the right side), for both T_1 and S_1, is more concentrated in the 6-member rings. b) Illustration of the shortest donor-acceptor distances (R_L), the average value was used in the intramolecular energy transfer analysis (subsection 4.3 Intramolecular energy transfer rates).

4.2 Intensity parameters

The Forced Electric Dipole (FED – Judd-Ofelt theory) and the Dynamic Coupling (DC) mechanisms are the most effective mechanisms for the $4f$-$4f$ intensities when the lanthanide occupies a non-centrosymmetric site.[5–7] The theoretical expressions for the intensity parameters, Ω_λ^{theo} ($\lambda = 2, 4, and\ 6$), have been described in detail in several references [8–13]. Here a brief recall is given:

$$\Omega_\lambda^{theo} = (2\lambda + 1) \sum_{t,p} \frac{|B_{\lambda tp}|^2}{2t + 1} \quad , \qquad B_{\lambda tp} = B_{\lambda tp}^{FED} + B_{\lambda tp}^{DC} \tag{S1}$$

where,

$$B_{\lambda tp}^{FED} = \frac{2}{\Delta E}\langle r^{t+1}\rangle\Theta(t,\lambda)\left(\frac{4\pi}{2t+1}\right)^{\frac{1}{2}}\sum_j \frac{e^2\rho_j g_j(2\beta_j)^{t+1}}{R_j^{t+1}}(Y_p^{t*})_j \tag{S2}$$

$$B_{\lambda tp}^{DC} = -\left[\frac{(\lambda+1)(2\lambda+3)}{(2\lambda+1)}\right]^{\frac{1}{2}}\langle r^\lambda\rangle\langle f\|C^{(\lambda)}\|f\rangle\left(\frac{4\pi}{2t+1}\right)^{\frac{1}{2}} \times\times \sum_j \frac{[(2\beta_j)^{t+1}\alpha_{OP,j}+\alpha_j']}{R_j^{t+1}}(Y_p^{t*})_j\delta_{t,\lambda+1} \tag{S3}$$

with t and p being the ranks and components of the spherical harmonics (Y_p^{t*}), $\langle f\|C^{(2)}\|f\rangle = -1.366$, $\langle f\|C^{(4)}\|f\rangle = 1.128$, $\langle f\|C^{(6)}\|f\rangle = -1.27$, ρ is the overlap integral between the valence subshells of the ligating atom and the $4f$ subshell of the lanthanide ion [14], $\beta = 1/(1\pm\rho)$ is a parameter that defines the centroid of the electronic density of the chemical bond Ln–X (X= ligating atom), α' is the effective polarizability from each ligand around the Ln^{3+} ion.

Eq. S2 is the expression of the Simple Overlap Model (SOM) for the odd part of the ligand field [11,12] and the charge factor g represents, by means of the product $-e\rho g$, the shared charged between the lanthanide $4f$ and the ligating atom valence orbitals. In the present work, g was considered equal to 1. The Bond Overlap Model (BOM, Eq. S3) for the Dynamic Coupling mechanism also takes into account the covalency effect by the overlap polarizabilities α_{OP} [15]. These quantities are closely related to the covalent fraction of a chemical bond [16–18] and can be estimated by:

$$\alpha_{OP} = \frac{e^2\rho^2 R^2}{2\Delta\varepsilon} \tag{S4}$$

where e is the electron charge, R is the length of the bond, and $\Delta\varepsilon$ is the excitation energy associated with the chemical bond.

The JOYSpectra program[19] was employed to calculate the Ω_λ^{theo} and their FED contributions (Ω_λ^{FED}) that are essential for estimates of the intramolecular energy transfer rate by the dipole-dipole mechanism (Eq. S5). Thus, the set of Ω_λ^{FED} obtained (in units of 10^{-20} cm^2) is: $\Omega_2^{FED} = 0.020$; $\Omega_4^{FED} = 0.250$; $\Omega_6^{FED} = 0.482$.

4.3 Intramolecular energy transfer rates

Intramolecular energy transfer (IET) rates were calculated taking into account individual mechanisms, namely: dipole-dipole (W_{d-d}), dipole-multipole (W_{d-m}), and exchange (W_{ex}). These mechanisms are calculated according to Eqs. S5–S7.[13,20] These calculations also take into consideration the selection rules on J quantum number, which are of paramount importance in interpreting experimental results.[13]

The dipole-dipole contribution can be calculated as,

$$W_{d-d} = \frac{S_L(1-\sigma_1)^2 4\pi e^2}{(2J+1)G \ \hbar \ R_L^6} \sum_K \Omega_K^{FED} \langle \psi^* J^* \| U^{(K)} \| \psi J \rangle^2 F \tag{S5}$$

where the intensity parameters Ω_K^{FED} were estimated in subsection **4.2 Intensity parameters**.

The dipole-multipole mechanism (2^K-pole, $K = 2, 4,$ and 6) is calculated as,

$$W_{d-m} = \frac{S_L}{(2J+1)G} \frac{2\pi e^2}{\hbar} \sum_K (K+1) \frac{\langle r^K \rangle^2}{\left(R_L^{K+2}\right)^2} \langle f \| C^{(K)} \| f \rangle^2 (1-\sigma_K)^2 \langle \psi^* J^* \| U^{(K)} \| \psi J \rangle^2 F \tag{S6}$$

The exchange mechanism is very sensitive to short-range distances, it can be calculated as

$$W_{ex} = \frac{(1-\sigma_0)^2 8\pi e^2}{(2J+1)G3\hbar R_L^4} \langle \psi^* J^* \| S \| \psi J \rangle^2 \sum_m \left| \left\langle \phi \left| \sum_j \mu_z(j) s_m(j) \right| \phi^* \right\rangle \right|^2 F \tag{S7}$$

In the above equations, R_L is the donor-acceptor states distance, estimated in subsection **4.1 In silico experiments**. The values of the squared reduced matrix elements $\langle \psi' J' \| U^{(\lambda)} \| \psi J \rangle^2$ are from Carnall et al.[21]. S_L is the dipole strength of the ligand transition involved in IET (10^{-36} and 10^{-40} $(esu)^2 cm^2$ for S_1 and T_1, respectively[13]), the $\langle r^\lambda \rangle$ are the $4f$ radial integrals[22,23], G is the ligand state degeneracy ($G = 1$ or 3 for S_1 or T_1, respectively), $\langle f \| C^{(\lambda)} \| f \rangle$ is the reduced matrix element of Racah's tensor operators.

In Eq. S7, s_m is the spin operator in the ligand and μ_z is the dipole operator (its z-component), the value of the element matrix of these coupled operators is in the order of 10^{-36} $(esu)^2 cm^2$.[13,24] The $\langle \psi' J' \| S \| \psi J \rangle$ is the reduced matrix elements of the spin operator, which were calculated using free-ion wavefunctions in the intermediate coupling scheme.[25,26]

The shielding factors $(1-\sigma_K)$ are important quantities which are related with the overlap integrals ρ between the valence orbitals of the pair Ln–X (X is the ligating atom in the coordination sphere) and they are calculated using the following expressions,[14,27]

$$(1-\sigma_K) = \begin{cases} \rho(2\beta)^{K+1} & for \ K \neq 0 \\ \rho\left(\dfrac{R_{min}}{R_L}\right)^{7/2} & for \ K = 0 \end{cases} \tag{S8}$$

where $\beta = (1 \pm \rho)^{-1}$ is the parameter which defines the centroid of the Ln-X overlap[11] and R_{min} is the Ln-X minimal distance in the first coordination sphere.

The F term Eqs. S5–S7 is the spectral overlap factor that considers the energy mismatch condition between donor and acceptor states.[13,20] For the case of ligand-to-metal energy transfer, F can be estimated by:

$$F = \frac{1}{\hbar\gamma_L}\sqrt{\frac{ln(2)}{\pi}}e^{-\left(\frac{\Delta}{\hbar\gamma_L}\right)^2 ln(2)} \qquad (S9)$$

where Δ is the band maximum energy difference between donor state and lanthanide ion acceptor state, $\Delta = E_D - E_{Ln}$. The γ_L is the bandwidth at half-height for the donor state, assumed here a typical value of $\gamma_L = 3000\ cm^{-1}$ for both S_1 and T_1 states.

The forward energy transfer rates (W) involving the Tb^{3+} ions as acceptors are calculated by the sum over Eqs. S5–S7 in the same pathway:

$$W = W_{d-d} + W_{d-m} + W_{ex} \qquad (S10)$$

If Δ is negative, for a given energy transfer pathway, W must be multiplied by the barrier factor $exp(\Delta/k_B T)$, where k_B is the Boltzmann constant and T is the temperature.

The IET rates from the ligands to the Tb^{3+} ion were calculated using 22 acceptors transitions, from the $^7F_6$ and $^7F_5$ as initial states to $^5D_4$, $^5D_3$, $^5G_6$, $^5F_5$, $^5G_5$, $^5G_4$, $^5H_7$, $^5H_6$, $^5H_5$, $^5L_{10}$, $^5L_6$ as final states, localized in the Tb^{3+} ion. In this sense, a total of 44 IET pathways (22 for $S_1 \rightarrow Tb^{3+}$ and 22 for $T_1 \rightarrow Tb^{3+}$) were calculated, as Table S6 shows. One can be noticed that in the specific case of the {Tb(**L**)(H$_2$O)}.H$_2$O, there are few pathways with acceptor states in good energy resonance with donors (Δ close to zero, *i.e.* pathways 8, 20, and 21), all of them pathways belong to the $S_1 \rightarrow Tb^{3+}$ energy transfer channel and only pathway 21 is relevant, with a contribution of ~31% to the W_S^b independent of the temperature. Therefore, this indicates that temperature changes do not affect the behavior of IET rates. The values of these rates from 12 to 300 K are shown in Table S7.

It is important to mention that the $^7F_5$ level is separated approximately by 2000 cm^{-1} from the ground $^7F_6$ level,[21] consequently, these levels are not so thermally coupled. However, the nonradiative decay $^7F_5 \rightarrow {}^7F_6$ has an abnormally long lifetime, having a non-neglected population. This is the reason behind that the $^7F_5$ level can be considered as an acceptor level.[26,28–30]

Table S6. IET rates for the {Tb(**L**)(H$_2$O)}.H$_2$O. Δ is the energy difference between donor and acceptor states (in cm^{-1}). W_{d-d}, W_{d-m}, and W_{ex} are rates for the dipole-dipole, dipole–multipole, and exchange energy transfer mechanisms (in s^{-1}), respectively. W is the sum over them in each pathway while W^b is the corresponding backward (from acceptor to donor) energy transfer rate, they are multiplied by the barrier factor $exp(-|\Delta|/k_BT)$ if Δ is negative (k_B is the Boltzmann's constant and $T = 300\ K$). W_S (W_S^b) and W_T (W_T^b) are the total forward (backward) energy transfer rates from the S$_1$ and T$_1$ states.

Pathway Label	Donor	Acceptor	Δ	W_{d-d}	W_{d-m}	W_{ex}	W	W^b
1	S$_1$	$^7F_6\rightarrow{}^5D_4$	10806	3.32×10^{-2}	3.94	0.00	3.97	1.24×10^{-22}
2	S$_1$	$^7F_6\rightarrow{}^5D_3$	5014	3.31×10^1	3.19	0.00	3.63×10^1	1.31×10^{-9}
3	S$_1$	$^7F_6\rightarrow{}^5G_6$	4827	3.00×10^3	9.44×10^3	2.15×10^6	2.16×10^6	1.91×10^{-4}
4	S$_1$	$^7F_6\rightarrow{}^5L_{10}$	4279	2.16×10^3	1.70×10^1	0.00	2.18×10^3	2.67×10^{-6}
5	S$_1$	$^7F_6\rightarrow{}^5G_5$	3483	8.43×10^2	1.66×10^4	2.39×10^4	4.14×10^4	2.30×10^{-3}
6	S$_1$	$^7F_6\rightarrow{}^5G_4$	2963	6.87×10^2	1.81×10^3	0.00	2.49×10^3	1.68×10^{-3}
7	S$_1$	$^7F_6\rightarrow{}^5L_6$	1640	0.00	0.00	2.73×10^3	2.73×10^3	1.05
8	S$_1$	$^7F_6\rightarrow{}^5H_7$	-129	0.00	0.00	4.17×10^3	2.25×10^3	4.17×10^3
9	S$_1$	$^7F_6\rightarrow{}^5H_6$	-1641	0.00	0.00	2.21×10^5	8.43×10^1	2.21×10^5
10	S$_1$	$^7F_6\rightarrow{}^5H_5$	-2517	0.00	0.00	2.03×10^{-11}	1.16×10^{-16}	2.03×10^{-11}
11	S$_1$	$^7F_6\rightarrow{}^5F_5$	-3684	0.00	0.00	4.01×10^5	8.52×10^{-3}	4.01×10^5
12	S$_1$	$^7F_5\rightarrow{}^5D_4$	12854	1.85×10^{-3}	1.76	3.85×10^{-1}	2.14	3.61×10^{-27}
13	S$_1$	$^7F_5\rightarrow{}^5D_3$	7062	1.19×10^1	4.54×10^2	0.00	4.65×10^2	9.10×10^{-13}
14	S$_1$	$^7F_5\rightarrow{}^5G_6$	6875	5.16×10^1	4.37×10^3	6.91×10^3	1.13×10^4	5.43×10^{-11}
15	S$_1$	$^7F_5\rightarrow{}^5L_{10}$	6327	1.24×10^1	5.27×10^{-2}	0.00	1.24×10^1	8.25×10^{-13}
16	S$_1$	$^7F_5\rightarrow{}^5G_5$	5531	1.13×10^2	3.97×10^2	2.77×10^5	2.78×10^5	8.39×10^{-7}
17	S$_1$	$^7F_5\rightarrow{}^5G_4$	5011	5.52×10^1	3.00×10^3	6.80×10^3	9.85×10^3	3.60×10^{-7}
18	S$_1$	$^7F_5\rightarrow{}^5L_6$	3688	0.00	0.00	2.59×10^1	2.59×10^1	5.39×10^{-7}
19	S$_1$	$^7F_5\rightarrow{}^5H_7$	1919	0.00	0.00	0.00	0.00	0.00
20	S$_1$	$^7F_5\rightarrow{}^5H_6$	407	0.00	0.00	5.29×10^3	5.29×10^3	7.51×10^2
21	S$_1$	$^7F_5\rightarrow{}^5H_5$	-469	0.00	0.00	8.23×10^5	8.68×10^4	8.23×10^5
22	S$_1$	$^7F_5\rightarrow{}^5F_5$	-1636	0.00	0.00	1.19×10^6	4.67×10^2	1.19×10^6
						W_S	$\mathbf{2.60\times10^6}$	-
						W_S^b	-	$\mathbf{2.64\times10^6}$
23	T$_1$	$^7F_6\rightarrow{}^5D_4$	2283	1.79	2.12×10^2	0.00	2.14×10^2	3.76×10^{-3}
24	T$_1$	$^7F_6\rightarrow{}^5D_3$	-3509	8.88×10^{-1}	8.58×10^{-2}	0.00	4.79×10^{-8}	9.74×10^{-1}
25	T$_1$	$^7F_6\rightarrow{}^5G_6$	-3696	6.30×10^1	1.98×10^2	4.51×10^6	9.05×10^{-2}	4.51×10^6
26	T$_1$	$^7F_6\rightarrow{}^5L_{10}$	-4244	2.21×10^1	1.74×10^{-1}	0.00	3.23×10^{-8}	2.23×10^1
27	T$_1$	$^7F_6\rightarrow{}^5G_5$	-5040	3.04	5.99×10^1	8.60×10^3	2.76×10^{-7}	8.67×10^3
28	T$_1$	$^7F_6\rightarrow{}^5G_4$	-5560	1.25	3.29	0.00	1.19×10^{-11}	4.53
29	T$_1$	$^7F_6\rightarrow{}^5L_6$	-6883	0.00	0.00	8.74×10^1	4.04×10^{-13}	8.74×10^1
30	T$_1$	$^7F_6\rightarrow{}^5H_7$	-8652	0.00	0.00	1.31×10^1	1.25×10^{-17}	1.31×10^1
31	T$_1$	$^7F_6\rightarrow{}^5H_6$	-10164	0.00	0.00	9.52×10^1	6.45×10^{-20}	9.52×10^1
32	T$_1$	$^7F_6\rightarrow{}^5H_5$	-11040	0.00	0.00	2.77×10^{-15}	2.81×10^{-38}	2.77×10^{-15}
33	T$_1$	$^7F_6\rightarrow{}^5F_5$	-12207	0.00	0.00	1.18×10^1	4.45×10^{-25}	1.18×10^1
34	T$_1$	$^7F_5\rightarrow{}^5D_4$	4331	1.24	1.18×10^3	3.05×10^4	3.17×10^4	3.02×10^{-5}
35	T$_1$	$^7F_5\rightarrow{}^5D_3$	-1461	3.97	1.52×10^2	0.00	1.41×10^{-1}	1.56×10^2
36	T$_1$	$^7F_5\rightarrow{}^5G_6$	-1648	1.35×10^1	1.14×10^3	2.14×10^5	7.94×10^1	2.15×10^5
37	T$_1$	$^7F_5\rightarrow{}^5L_{10}$	-2196	1.58	6.71×10^{-3}	0.00	4.23×10^{-5}	1.58
38	T$_1$	$^7F_5\rightarrow{}^5G_5$	-2992	5.05	1.78×10^1	1.47×10^6	8.62×10^{-1}	1.47×10^6
39	T$_1$	$^7F_5\rightarrow{}^5G_4$	-3512	1.25	6.80×10^1	1.82×10^4	8.85×10^{-4}	1.82×10^4
40	T$_1$	$^7F_5\rightarrow{}^5L_6$	-4835	0.00	0.00	1.22×10^1	1.04×10^{-9}	1.22×10^1
41	T$_1$	$^7F_5\rightarrow{}^5H_7$	-6604	0.00	0.00	0.00	0.00	0.00
42	T$_1$	$^7F_5\rightarrow{}^5H_6$	-8116	0.00	0.00	3.36×10^1	4.19×10^{-16}	3.36×10^1
43	T$_1$	$^7F_5\rightarrow{}^5H_5$	-8992	0.00	0.00	1.65×10^3	3.09×10^{-16}	1.65×10^3
44	T$_1$	$^7F_5\rightarrow{}^5F_5$	-10159	0.00	0.00	5.18×10^2	3.59×10^{-19}	5.18×10^2
						W_T	$\mathbf{3.20\times10^4}$	-
						W_T^b	-	$\mathbf{6.22\times10^6}$

Table S7. Total forward and backward IET rates (in s^{-1}) and lifetimes* (in ms) with the change of temperature for the $\{Tb(\mathbf{L})(H_2O)\}.H_2O$ material. The τ_S was fixed at 10^{-6} s **.

Temperature (K)	W_S	W_S^b	W_T	W_T^b	τ_4	τ_T
16	2.51×10^6	2.64×10^6	3.19×10^4	6.22×10^6	0.28	604.17
20	2.51×10^6	2.64×10^6	3.19×10^4	6.22×10^6	0.28	704.47
50	2.51×10^6	2.64×10^6	3.19×10^4	6.22×10^6	0.29	682.66
100	2.51×10^6	2.64×10^6	3.19×10^4	6.22×10^6	0.31	698.71
150	2.52×10^6	2.64×10^6	3.19×10^4	6.22×10^6	0.31	419.50
200	2.54×10^6	2.64×10^6	3.19×10^4	6.22×10^6	0.33	123.14
250	2.57×10^6	2.64×10^6	3.19×10^4	6.22×10^6	0.31	–
275	2.59×10^6	2.64×10^6	3.19×10^4	6.22×10^6	0.32	–
300	2.60×10^6	2.64×10^6	3.20×10^4	6.22×10^6	0.31	–

* Experimentally measured.
** Since the S_1 can be observed within a delay of 10^{-5} s, as shown by the time-resolved emission spectra excited at 270 nm in Figure S8, this value may be acceptable.

4.4 Rate equations

Based on the IET rates and the schematic energy level diagram (Figure 7), is possible to construct an appropriate set of ordinary differential equations (ODEs) with boundary conditions and solve it from the initial state (t = 0 s) until reaching the steady-state regime, where all states are in a dynamic equilibrium. To simplify the setup of the rate equations, groups of levels are represented in brackets |n⟩ (as depicted in Figure 7) and their respective population as P_n. Thus, a 5-level set of ODEs with initial conditions (when t = 0 s) is given by:

ODE	**Initial condition**	**Level (or Levels)**	
$\frac{d}{dt}P_1(t) = -\left(\frac{1}{\tau_T} + W_T\right)P_1(t) + W_{ISC}P_2(t) + W_T^b P_3(t)$	$P_1(0) = 0$	T_1	(S11)
$\frac{d}{dt}P_2(t) = -\left(\frac{1}{\tau_S} + W_{ISC} + W_S\right)P_2(t) + \phi P_0(t) + W_S^b P_3(t)$	$P_2(0) = 0$	S_1	(S12)
$\frac{d}{dt}P_3(t) = -\left(W_{3\to4} + W_T^b + W_S^b\right)P_3(t) + W_S P_2(t)$	$P_3(0) = 0$	$^5D_3$ to $^5F_5$	(S13)

$$\frac{d}{dt}P_4(t) = -\left(\frac{1}{\tau_4}\right)P_4(t) + W_{3\to4}P_3(t) + W_T P_1(t) \qquad\qquad P_4(0) = 0 \qquad {}^5D_4 \qquad \text{(S14)}$$

$$\frac{d}{dt}P_0(t) = -\phi P_0(t) + \frac{1}{\tau_T}P_1(t) + \frac{1}{\tau_S}P_2(t) + \frac{1}{\tau_4}P_4(t) \qquad\qquad P_0(0) = 1 \qquad S_0 \text{ and } {}^7F_6 \qquad \text{(S15)}$$

where τ_T, τ_S, and τ_4 are the lifetimes of the T_1, S_1, and ${}^5D_4$ levels, respectively. W_{ISC} is the intersystem crossing rate $S_1 \to T_1$, which is sensitive to the energy gap between the S_1 and T_1 state [31] and, in the present case, such energy gap of ~8500 cm^{-1} may lead to a reasonable value of W_{ISC}~10^6 s^{-1}.[32,33] $W_{3\to4}$ is the nonradiative decay from upper levels of Tb^{3+} to the emitting ${}^5D_4$ level that is in the order of ~10^6 s^{-1} for Ln^{3+}-chelates.[13] W_T and W_S are the forward ligand-to-Tb energy transfer rates while the backward Tb-to-ligand rates are represented by a superscript b (W_T^b and W_S^b), see Table S7.

The pumping rate ϕ~136 s^{-1} was estimated using,

$$\phi = \frac{\sigma \rho \lambda_{exc}}{hc} \tag{S16}$$

where σ (~10^{-16} cm^2) is the absorption cross-section of the organic ligands, ρ (~ 1 W/cm^2) is the power density of the excitation source at λ_{exc} = 270 nm. The h and c are the constants of Planck and the speed of light. If the power density is increased (*e.g.* ρ = 10 W/cm^2, leading to ϕ~1360 s^{-1}), it will reflect in a higher depopulation of the ground-level (P_0, Eq. S15) and, of course, increasing mainly the populations of T_1 and ${}^5D_4$ levels. However, at the equilibrium, the ratio between the populations P_n ($n \neq 0$, the ground-level) are the same as those with ρ = 1 W/cm^2. This makes the population analysis of the T_1 and ${}^5D_4$ independent of the power density.

The ODEs (Eqs. S11–S15) were solved using the fourth-order Runge-Kutta method with adaptive stepsize.[34]

Table S8. Population fractions in the steady-state regime for the 5-levels system represented as represented in Figure 7.

Temperature (K)	P_1	P_2	P_3	P_4	P_0
16	2.79×10^{-3}	3.45×10^{-5}	8.78×10^{-6}	2.77×10^{-2}	9.69×10^{-1}
20	2.79×10^{-3}	3.45×10^{-5}	8.78×10^{-6}	2.70×10^{-2}	9.70×10^{-1}
50	2.79×10^{-3}	3.44×10-5	8.77×10^{-6}	2.85×10^{-2}	9.69×10^{-1}

|					
100	2.79×10^{-3}	3.44×10^{-5}	8.76×10^{-6}	3.00×10^{-2}	9.67×10^{-1}
150	2.79×10^{-3}	3.43×10^{-5}	8.77×10^{-6}	2.98×10^{-2}	9.67×10^{-1}
200	2.78×10^{-3}	3.41×10^{-5}	8.79×10^{-6}	3.22×10^{-2}	9.65×10^{-1}
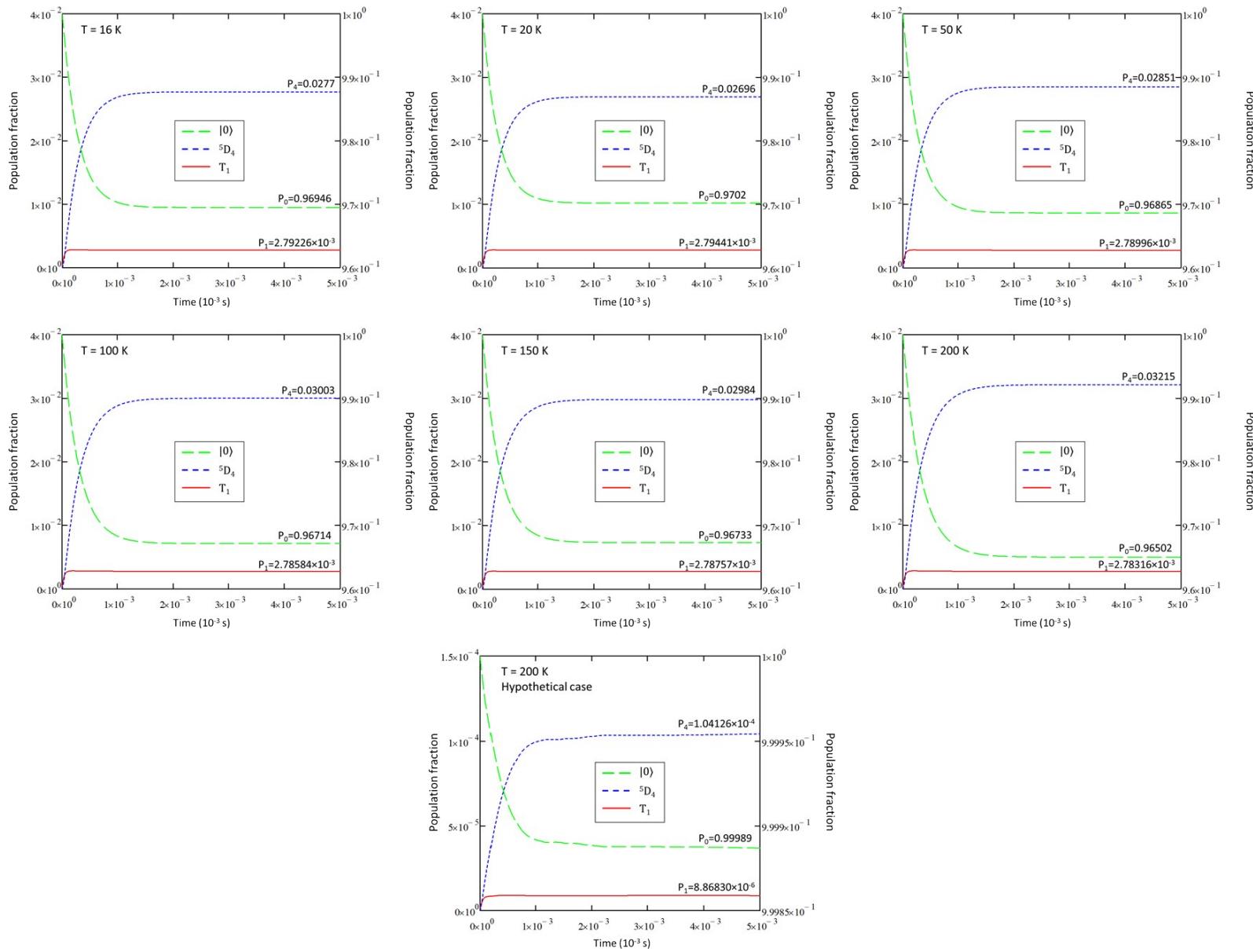
Figure S14. Population fraction as a function of time for the $^5D_4$, T_1, (both left-side scale) and the ground state $|0\rangle$ (right-side scale) when the temperature is changed from 16 to 200 K. The hypothetical case, where the τ_T and τ_S are shorter, is illustrated in the last graph at the bottom.

References

1   M. J. Frisch, G. W. Trucks, H. B. Schlegel, G. E. Scuseria, M. A. Robb, J. R. Cheeseman, G. Scalmani, V. Barone, B. Mennucci, G. A. Petersson, H. Nakatsuji, M. Caricato, X. Li, H. P. Hratchian, A. F. Izmaylov, J. Bloino, G. Zheng, J. L. Sonnenberg, M. Hada, M. Ehara, K. Toyota, R. Fukuda, J. Hasegawa, M. Ishida, T. Nakajima, Y. Honda, O. Kitao, H. Nakai, T. Vreven, J. J. A. Montgomery, J. E. Peralta, F. Ogliaro, M. Bearpark, J. J. Heyd, E. Brothers, K. N. Kudin, V. N. Staroverov, T. Keith, R. Kobayashi, J. Normand, K. Raghavachari, A. Rendell, J. C. Burant, S. S. Iyengar, J. Tomasi, M. Cossi, N. Rega, J. M. Millam, M. Klene, J. E. Knox, J. B. Cross, V. Bakken, C. Adamo, J. Jaramillo, R. Gomperts, R. E. Stratmann, O. Yazyev, A. J. Austin, R. Cammi, C. Pomelli, J. W. Ochterski, R. L. Martin, K. Morokuma, V. G. Zakrzewski, G. A. Voth, P. Salvador, J. J. Dannenberg, S. Dapprich, A. D. Daniels, O. Farkas, J. B. Foresman, J. V. Ortiz, J. Cioslowski and D. J. Fox, Gaussian 09, revision D.01, 2013.

2   C. Lee, W. Yang and R. G. Parr, *Phys. Rev. B*, 1988, **37**, 785–789.

3   A. D. Becke, *J. Chem. Phys.*, 1993, **98**, 5648–5652.

4   R. Krishnan, J. S. Binkley, R. Seeger and J. A. Pople, *J. Chem. Phys.*, 1980, **72**, 650–654.

5   B. R. Judd, *Phys. Rev.*, 1962, **127**, 750–761.

6   G. S. Ofelt, *J. Chem. Phys.*, 1962, **37**, 511–520.

7   C. K. Jørgensen and B. R. Judd, *Mol. Phys.*, 1964, **8**, 281–290.

8   B. G. Wybourne, *Spectroscopic Properties of Rare Earths*, John Wiley & Sons, 1965.

9   G. F. de Sá, O. L. Malta, C. de Mello Donegá, A. M. Simas, R. L. Longo, P. A. Santa-Cruz and E. F. da Silva, *Coord. Chem. Rev.*, 2000, **196**, 165–195.

10   R. T. Moura, A. N. Carneiro Neto, R. L. Longo and O. L. Malta, *J. Lumin.*, 2016, **170**, 420–430.

11   O. L. Malta, *Chem. Phys. Lett.*, 1982, **88**, 353–356.

12   O. L. Malta, *Chem. Phys. Lett.*, 1982, **87**, 27–29.

13   A. N. Carneiro Neto, E. E. S. Teotonio, G. F. de Sá, H. F. Brito, J. Legendziewicz, L. D. Carlos, M. C. F. C. Felinto, P. Gawryszewska, R. T. Moura Jr., R. L. Longo, W. M. Faustino and O. L. Malta, in *Handbook on the Physics and Chemistry of Rare Earths, volume 56*, Elsevier, 2019, pp. 55–162.

14   A. N. Carneiro Neto and R. T. Moura Jr., *Chem. Phys. Lett.*, 2020, **757**, 137884.

15   R. T. Moura Jr, A. N. Carneiro Neto, R. L. Longo and O. L. Malta, *J. Lumin.*, 2016, **170**, 420–430.

16   O. L. Malta, H. J. Batista and L. D. Carlos, *Chem. Phys.*, 2002, **282**, 21–30.

17   R. T. Moura, O. L. Malta and R. L. Longo, *Int. J. Quantum Chem.*, 2011, **111**, 1626–1638.

18   R. T. Moura Jr., G. C. S. Duarte, T. E. da Silva, O. L. Malta and R. L. Longo, *Phys. Chem. Chem. Phys.*, 2015, **17**, 7731–7742.

19   A. N. Carneiro Neto, E. C. Aguiar, C. V. Santos-Jr., E. M. de Lima, A. Shyichuk, E. E. S. Teotonio, W. M. Faustino, H. F. Brito, M. C. F. C. Felinto, R. A. S. Ferreira, R. L. Longo, L. D. Carlos, O. L. Malta and R. T. Moura Jr., *To be Submitt.*

20   O. L. Malta, *J. Lumin.*, 1997, **71**, 229–236.

21   W. T. Carnall, H. Crosswhite and H. M. Crosswhite, *Energy level structure and transition probabilities in the spectra of the trivalent lanthanides in LaF₃*, Argonne, IL (United States), IL (United States), 1978.

22   S. Edvardsson and M. Klintenberg, *J. Alloys Compd.*, 1998, **275–277**, 230–233.

23   L. Smentek, *Phys. Rep.*, 1998, **297**, 155–237.

24   F. R. G. e Silva and O. L. Malta, *J. Alloys Compd.*, 1997, **250**, 427–430.

25   G. S. Ofelt, *J. Chem. Phys.*, 1963, **38**, 2171–2180.

26   E. Kasprzycka, A. N. Carneiro Neto, V. A. Trush, L. Jerzykiewicz, V. M. Amirkhanov, O. L. Malta, J. Legendziewicz and P. Gawryszewska, *J. Rare Earths*, 2020, **38**, 552–563.

27   O. L. Malta, *J. Non. Cryst. Solids*, 2008, **354**, 4770–4776.

28   K. Rademaker, W. F. Krupke, R. H. Page, S. A. Payne, K. Petermann, G. Huber, A. P. Yelisseyev, L. I. Isaenko, U. N. Roy, A. Burger, K. C. Mandal and K. Nitsch, *J. Opt. Soc. Am. B*, 2004, **21**, 2117.

29   U. N. Roy, R. H. Hawrami, Y. Cui, S. Morgan, A. Burger, K. C. Mandal, C. C. Noblitt, S. A. Speakman, K. Rademaker and S. A. Payne, *Appl. Phys. Lett.*, 2005, **86**, 151911.

30   A. S. Souza, L. A. Nunes, M. C. F. C. Felinto, H. F. Brito and O. L. Malta, *J. Lumin.*, 2015, **167**, 167–171.

31   M. J. Beltrán-Leiva, E. Solis-Céspedes and D. Páez-Hernández, *Dalt. Trans.*, 2020, **49**, 7444–7450.

32   M. A. El-Sayed, *J. Chem. Phys.*, 1963, **38**, 2834–2838.

33   M. Kasha, *Discuss. Faraday Soc.*, 1950, **9**, 14.

34   W. Press, S. Teukolsky, W. Vetterling, B. Flannery, E. Ziegel, W. Press, B. Flannery, S. Teukolsky and W. Vetterling, *Numerical Recipes: The Art of Scientific Computing*, 1987, vol. 29.